Transverse effects in multifrequency Raman generation

Syed, KS, Mcdonald, GS and New, GHC

http://dx.doi.org/10.1364/JOSAB.17.001366

Transverse effects in ultrabroadband multifrequency Raman generation

K. S. Syed, G. S. McDonald,* and G. H. C. New†

Laser Optics & Spectroscopy Group, The Blackett Laboratory, Imperial College of Science, Technology and Medicine, Prince Consort Road, London SW7 2BW, UK

Received October 13, 1999; revised manuscript received April 25, 2000

The theory of ultrabroadband multifrequency Raman generation is extended, for the first time, to allow for beam-propagation effects in one and two transverse dimensions. We show that a complex transverse structure develops even when diffraction is neglected. In the general case, we examine how the ultrabroadband multifrequency Raman generation process is affected by the intensity, phase quality, and width of the input beams, and by the length of the Raman medium. The evolution of power spectra, intensity profiles, and global characteristics of the multifrequency beams are investigated and explained. In the two-dimensional transverse case, bandwidths comparable to the optical carrier frequency, spanning the whole visible spectrum and beyond, are still achievable. © 2000 Optical Society of America [S0740-3224(00)01408-9]

OCIS codes: 190.2620, 190.4380, 190.4410, 190.4420, 290.5910.

1. INTRODUCTION

Ultrabroadband multifrequency Raman generation (UMRG) is unique among nonlinear optical interactions in terms of the number of distinct frequencies of *comparable* energy that can be generated.[1–13] UMRG differs from conventional Raman conversion schemes in that two input beams of comparable intensity and shape are employed whose frequency separation matches the highest-gain Raman resonance of the medium. This scheme is called resonant symmetric pumping, and its advantage is that a very wide comb of both Stokes and anti-Stokes components is rapidly generated.

With H_2 gas as the Raman medium, beams containing several tens of frequency components are possible, while air at atmospheric pressure has the potential for generating beams with well over 100 frequency channels.[5] Although transverse effects have received considerable attention in the context of conventional Raman geometries, the theory of UMRG has to date been based exclusively on plane-wave analyses. Given that narrow focused beams are regularly used to create high intensities in UMRG experiments, the role of beam-propagation effects clearly needs to be examined. In this paper we present the first theoretical investigation of UMRG in which transverse effects in one and two dimensions are taken into account.

2. MODEL EQUATIONS

To model transverse UMRG, the total electric field $E_T(x', y', z, t)$ is expanded in terms of a set of individual beams $F_n(x', y', z, t)$ whose carrier frequencies are given by $\omega_n = \omega_0 + n\omega_R$, where $n = 0, \pm 1, \pm 2, \ldots, \omega_0$ and ω_R are the pump frequency and the Stokes shift, respectively, and x', y', and z are the transverse and the longitudinal coordinates. We write $E_T(x', y', z, t) = \Sigma_n F_n(x', y', z, t)\exp[i(\omega_n t - k_n z)]$, in which F_n is a complex amplitude profile and k_n is the z component of the propagation vector of the nth beam; $k_n = \omega_n/c + \Delta k_n = k_n^0 + \Delta k_n$, and Δk_n is the momentum mismatch arising from dispersion. For a local time frame $t = t_{\mathrm{lab}} - z/c$, the coupled propagation equations take the form

$$\frac{\partial F_n}{\partial z} - \frac{i}{2k_n^0}\nabla_t'^2 F_n = \frac{\pi\rho\alpha_{12}\omega_n}{c} \times [q^* F_{n+1}\exp(-i\Delta_{n+1}z) - qF_{n-1}\exp(i\Delta_n z)]. \quad (1)$$

Here, $\nabla_t'^2$ is the (diffractive) transverse Laplacian, ρ is the molecular number density, a_{12} is a coupling constant determining the Raman gain (see below), $\Delta_n = (\Delta k_n - \Delta k_{n-1}) - (\Delta k_0 - \Delta k_{-1}) = (k_n - k_{n-1}) - (k_0 - k_{-1})$ is a composite momentum mismatch,[14,15] and q is a complex variable characterizing the state of the medium that evolves in time according to

$$\frac{\partial q}{\partial t} = -\frac{q}{T_2} + \frac{a_{12}}{2\hbar}\sum_j F_j F_{j-1}^* \exp(-i\Delta_j), \quad (2)$$

in which T_2 is the dephasing time of the medium. The variation of the refractive index of H_2 with frequency is assumed to follow a Cauchy-type dispersion relation: $\mu_n = 1 + \delta_0\Omega_0^2 d/(\Omega_0^2 - \omega_n^2)$, where d is gas density, $\delta_0 = 1.4 \times 10^{-4}$ amagat^{-1} is a constant, and $\Omega_0/2\pi c = 1.17 \times 10^{-5}$ cm^{-1} is an effective resonant frequency.[16] It is well known that n_2, the coefficient for nonlinear refraction, is particularly small for H_2 gas. For the purposes of this paper we include only linear refraction in the modeling, and hence self-focusing effects are assumed negligible. We consider pump beams derived from the second harmonic of a Nd-doped yttrium aluminum garnet laser ($\omega_0/2\pi c = 18\,900$ cm^{-1}) and a Raman sideband that is generated by conventional stimulated Raman scattering (SRS) techniques. At atmospheric

pressure and room temperature the Raman line with the highest gain coefficient ($g = 0.2$ cm GW^{-1}) corresponds to the $S(1)$ rotational transition ($\omega_R/2\pi c = 587$ cm^{-1}) and $T_2 \simeq 2$ ns.

It is convenient to recast Eqs. (1) and (2) into dimensionless form. We define constants $A = a_{12}T_2/2\hbar$ and $B = \pi\rho a_{12}\omega_0/c$ and the dimensionless variables: $\tau = t/t_p$, $Z = gI_0z$, $x = x'/w_p$, $y = y'/w_p$, $A_n = F_n/F_0$, and $P = q/AI_0$, where $g = 2AB$ (the gain coefficient at ω_0), F_0 is the peak amplitude of the pump field, $I_0 = |F_0|^2$, t_p is the input pulse width, and w_p is the half-width of a reference Gaussian beam. The set of normalized dispersive mistunings $\gamma_n = \Delta_n/gI_0$ is also introduced.

We now have a set of equations describing the propagation, in Z, of the nth normalized electric field envelope $A_n(x, y, Z, \tau)$ and an equation for the time evolution of the polarization wave P in the medium:

$$\frac{\partial A_n}{\partial Z} = i\alpha_n\nabla_t^2 A_n + \frac{\omega_n}{2\omega_0}[P^*A_{n+1} \times \exp(-i\gamma_{n+1}Z) - PA_{n-1}\exp(i\gamma_nZ)], \quad (3)$$

$$\frac{T_2}{t_p}\frac{\partial P}{\partial \tau} = -P + \sum_j A_jA_{j-1}^*\exp(-i\gamma_jZ), \quad (4)$$

where $\nabla_t^2 = \nabla_t'^2/w_p^2$ is a scaled transverse Laplacian and α_n characterizes diffraction at ω_n. To give an intuitive measure of the strength of diffraction at ω_0, and how this varies across the Raman spectrum, it is useful to consider the free-space propagation of a continuous-wave Gaussian beam in each of the frequency channels. At the pump frequency this beam would have a normalized diffraction length of $Z_D = gI_0L_D$, where $L_D = k_0{}^0w_p^2/2$ is the distance over which the beam broadens to twice its width. The corresponding diffraction length in the nth channel would be given by $L_D^{(n)} = (\omega_n/\omega_0)L_D$. Defining an SRS gain length as $L_R = 1/gI_0$, α_n can be expressed in terms of a ratio of lengths: $\alpha_n = L_R/4L_D^{(n)}$. These coefficients thus quantify the *relative* strength of diffraction and SRS in each frequency channel. For any particular configuration, where the system is evolved from $Z = 0$ to $Z = Z_{\max}$ (i.e., from $z = 0$ to $z = z_{\max}$), the *absolute* level of diffraction can be deduced from the value of $Z_{\max}/Z_D = z_{\max}/L_D$.

The simultaneous solution of a very large number of coupled four-dimensional equations clearly presents an insurmountable computational challenge in terms of the requirements of both time and memory. However, we found in earlier work[2] that UMRG is generally most effective when t_p is larger than approximately $8T_2$ and that this quasi-steady-state regime can be accurately modeled by considering the limit $T_2/t_p \to 0$. In this paper we thus investigate transverse UMRG under steady-state conditions by setting

$$P = \sum_j A_jA_{j-1}^*\exp(-i\gamma_jZ). \quad (5)$$

Equation (3) is solved numerically using a split-step Fourier method[17] in which each Laplacian is implemented in the spatial-frequency domain whereas other terms are solved in real space by finite-difference techniques. The solution of the steady-state model still demands exceptionally large resources, so only one transverse coordinate is considered before progressing to simulations of the full two-dimensional (2D) transverse model. We will show that even in the one-dimensional (1D) system, transverse effects can result in quite dramatic modifications to the predictions of plane-wave theory. Moreover, although 2D simulations are strictly necessary to obtain accurate quantitative results, it will be shown that 1D transverse modeling yields surprising good overall agreement with results of the higher-dimensional system.

3. PLANE-WAVE ULTRABROADBAND MULTIFREQUENCY RAMAN GENERATION

In this section, key results from the steady-state plane-wave system ($\alpha_n = 0$) are presented. This permits the introduction of terminology and concepts that are necessary to interpret the more complex behaviors of the 1D and 2D transverse solutions. In conventional SRS, a single intense beam at the pump frequency ω_0 is converted to a Stokes beam frequency $\omega_{-1} = \omega_0 - \omega_R$. For high dispersion, and before significant depletion of the input energy, this process is described by

$$\frac{dA_{-1}}{dZ} = \frac{\omega_{-1}}{2\omega_0}|A_0|^2A_{-1} = \frac{\omega_{-1}}{2\omega_0}A_{-1} \simeq \frac{1}{2}A_{-1}, \quad (6)$$

yielding $|A_{-1}(Z)|^2 \simeq |A_{-1}(0)|^2\exp(Z)$ and thus exponential amplification of an existing Stokes wave $A_{-1}(0)$. Taking pump depletion into account, one arrives at the sequence of events depicted in Fig. 1(a). Typically,[18] the threshold for generating a Stokes wave from background noise to a level of 1% of the pump energy is $Z = Z_{\text{th}} \simeq 25$. Once the Stokes wave is established, it can lead to the generation of a second Stokes component at $\omega_{-2} = \omega_{-1} - \omega_R$, and so on. This cascade of frequency generation is nonparametric because each new frequency is required to exist at some level so that it can be amplified. Energy is transferred only to lower frequencies and, at any one distance, there can be at most only two distinct waves of comparable energy. Thus the generation of a spectrum of many frequencies is not possible with this configuration.

Generalizing considerations to a three-wave system, and a small but finite level of dispersion ($\gamma_1 \ll 1$), one arrives at the following expressions governing the evolution of the Stokes, pump, and anti-Stokes waves:

$$\frac{dA_{-1}}{dZ} = \frac{\omega_{-1}}{2\omega_0}[|A_0|^2A_{-1} + A_1^*A_0{}^2\exp(i\gamma_1Z)], \quad (7)$$

$$\frac{dA_0}{dZ} = \frac{1}{2}(|A_1|^2 - |A_{-1}|^2)A_0, \quad (8)$$

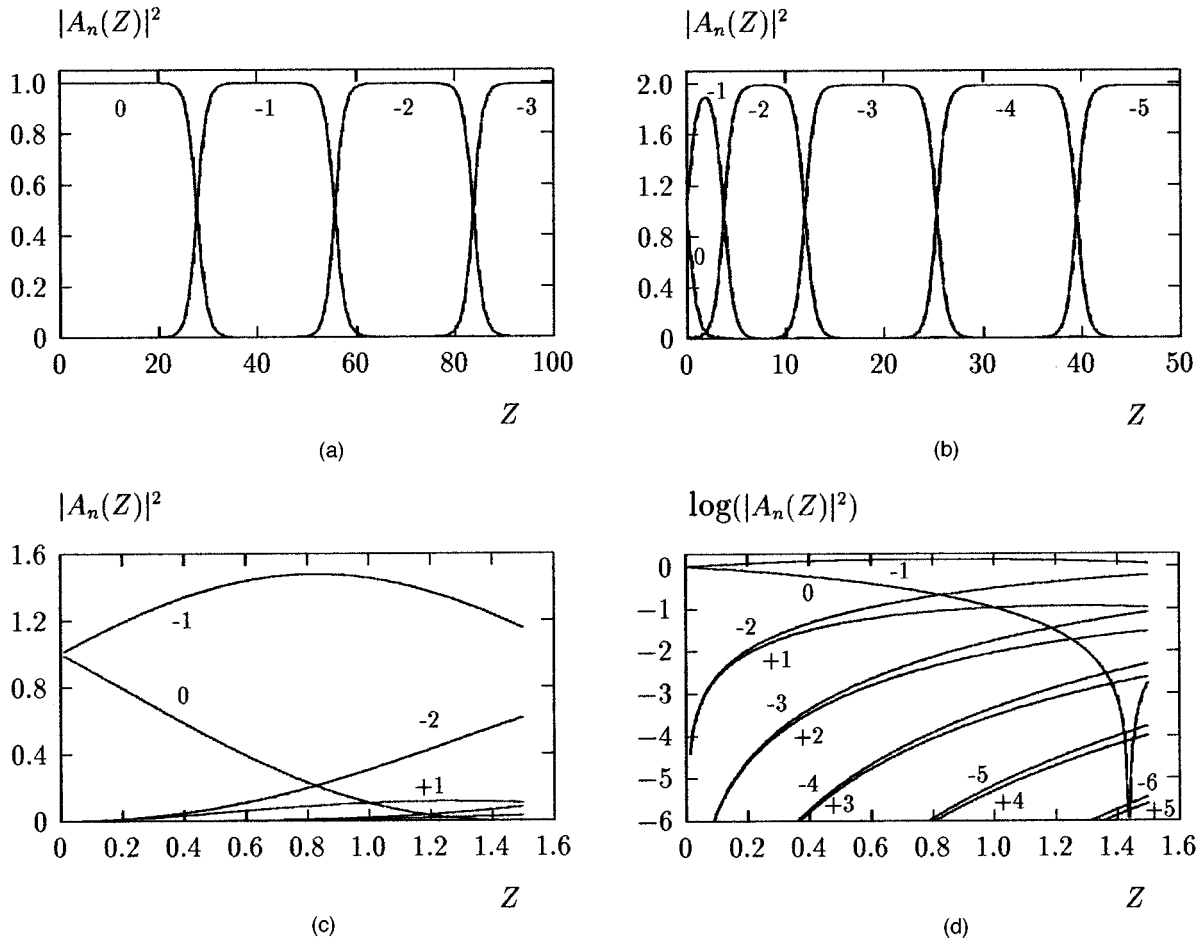

Fig. 1. Evolution of plane-wave intensities at distinct frequencies as a function of normalized propagation distance; individual curves are labeled with the appropriate channel number n: (a) conventional (single pump beam) stimulated Raman scattering (SRS); (b)–(d) the effect of symmetric two-color pumping. (b) High dispersion ultimately results in a single (nonparametric) downconversion ladder that is similar to conventional SRS. (c),(d) A low level of dispersion; significant parametric conversion over a relatively short propagation distance is demonstrated.

$$\frac{dA_1}{dZ} = \frac{\omega_1}{2\omega_0}[-|A_0|^2 A_1 - A_{-1}{}^* A_0^2 \exp(i\gamma_1 Z)]. \quad (9)$$

Two types of terms can be distinguished on the right-hand side of Eqs. (7), (8), and (9): terms containing $|A_j|^2$, (e.g., $|A_j|^2 A_{j-1}$ or $-|A_j|^2 A_{j+1}$) represent nonparametric processes, whereas the remaining dispersion-dependent parametric terms involve two distinct waves generating a third and thus effect frequency conversion without the need for an initial seed.

In the limit of exact phase matching, $\gamma_1 = 0$, all three waves can be considered as real. If one then attempts to amplify a small Stokes seed using an intense pump wave, the parametric term in Eq. (9) gives rise to a negative anti-Stokes component. The second term on the right-hand side of the Stokes equation then results in attenuation of the seed that one is trying to amplify. The growth of an antiphase wave at ω_1 thus leads to an abrupt end to Stokes amplification. The way to avoid such suppression of the Stokes gain, and simultaneously allow anti-Stokes generation, is to introduce finite dispersion.[18] This dispersion has to be small so that the parametric terms oscillate sufficiently slowly that they can still make a contribution to the system.

While γ_1 has been defined as the axial dispersion for collinear waves, it can also be expressed in a slightly more general form for the three-wave system that encompasses noncollinear geometries: $\gamma_1 = |\mathbf{k}_1 + \mathbf{k}_{-1} - 2\mathbf{k}_0|/gI_0$. In later sections, when finite beams and diffraction are considered, we will continue to parametrize dispersion using γ_1 defined as a longitudinal mistuning. However, such angular phase-matching considerations will be built into the modeling and expressed through the transverse components of the wave vectors of the interacting fields. For many years it was believed that the most efficient way to generate multiple anti-Stokes waves was to include a small amount of *angular* dispersion in the system by injecting a *weak* Stokes wave at a finite angle to the pump beam.[19] One problem with this geometry is that noncollinear waves lead to a low interaction volume which, in turn, severely limits the number of waves that can be generated.

Let us now consider the consequences of launching two *collinear* waves of *equal* amplitude. To facilitate a direct comparison with SRS using a single pump beam, for the moment we will examine the case of input beams at the pump and the anti-Stokes frequencies, $A_1(Z = 0) = A_0(Z = 0) = 1$, even though in the remainder of this

paper we deal with symmetric pumping at ω_0 and ω_{-1}. Irrespective of the level of dispersion, in the initial stages of propagation, $dA_0/dZ \simeq |A_1|^2 A_0/2$ and $A_0(Z) \simeq 1 + Z/2$. This implies a rapid transfer of energy from the higher-frequency input beam to the one with lower frequency. In the particular case of low dispersion, $\gamma_1 \simeq 0$, one also has that

$$dA_{-1}/dZ \simeq A_1 A_0^2/2 \simeq 1/2. \tag{10}$$

This yields $A_{-1}(Z) \simeq Z/2$ and a threshold of 1% parametric conversion to the Stokes frequency of $Z_{\text{th}} \simeq 0.2$. A comparison of this value with the corresponding threshold for single-pump SRS, $Z_{\text{th}} \simeq 25$, immediately demonstrates the relative efficiency of frequency generation under two-color pumping. Expression (10) also quantifies the importance of symmetric pumping for strong parametric conversion.

To explore the consequences of some of the above considerations, we present results from simulations of the plane-wave model that include many Stokes and anti-Stokes components. First, we investigate the effect of two-color pumping in the high-dispersion regime ($\gamma_1 \simeq 10$). Setting $A_0 = A_{-1} = 1$ and all other waves to zero at $Z = 0$ gives the results shown in Fig. 1(b). While one might have suspected that two simultaneous down conversion cascades would have resulted, it is found that the initial transfer of energy to the lower-frequency input channel leads to a single ladder of conversions and thus a maximum of only two waves at any large Z. For the same initial conditions we now lower the level of dispersion to $\gamma_1 \simeq 0$ and allow parametric processes to make a significant contribution. Figure 1(c) shows that these processes result in the generation of numerous waves over relatively short propagation distances. Indeed, five distinct frequencies are clearly visible at $Z = 1.5$. A more detailed examination of this case, Fig. 1(d), confirms the prediction of $Z_{\text{th}} \simeq 0.2$ and demonstrates that a wide spectrum of *pairs* of frequencies is generated. The key differences between UMRG and geometries that use a weak seed and angular dispersion are thus that symmetric pumping maximizes the strength of parametric frequency generation and that collinear propagation allows this efficient conversion to continue to large Z.

4. ONE-DIMENSIONAL TRANSVERSE ULTRABROADBAND MULTIFREQUENCY RAMAN GENERATION

In this section the full complexity of transverse UMRG is constrained by allowing the spatial structure of the propagating fields to develop in only one transverse dimension. This particular system has a physical correspondence to frequency generation in a narrow gas-filled waveguide, and its modeling permits a thorough exploration of certain qualitative aspects of transverse UMRG. A relatively large number of transverse points can be used, typically 2048 in each frequency channel, and this also allows extensive checking of the required transverse sampling densities for each parameter regime.

The first, and perhaps the most fundamental, question to ask is whether diffraction is intrinsically detrimental to ultrabroadband light generation. One aspect of this is whether diffractive coupling, in combination with Raman nonlinearity of the medium, leads to the growth of any spontaneous transverse instabilities as the fields propagate. We tested for this possibility in the context of plane-wave pump fields. Because one would expect the characteristic transverse length of any instability to scale as $1/\sqrt{\alpha_n}$, investigations were performed for a wide range of diffractive coupling strengths. One strategy was to test whether finite numerical precision (representing a low level of background noise) could be selectively amplified and lead to spatial structure, even when no finite-beam effects were explicitly introduced into the system. However, no such spontaneous structure was found, and the results obtained were the same as those of plane-wave modeling with no transverse coupling. As a further test, the above investigations were repeated with each frequency channel initially flooded with white noise (at a level of $A_{\text{noise}} = 10^{-3}$, representing a strong seed for any instabilities). Once again, results were essentially identical to those of plane-wave theory; the evolution of the transverse noise structure that was imposed, and its spatial Fourier spectrum, were examined, and no evidence of selective noise amplification was found. We concluded there were no appreciable spatial modulational instabilities present in the system, at least within the regimes we proposed to study.

A second issue is whether finite-beam effects alone imply that the propagating fields develop a complex spatial structure. To investigate this, the case of UMRG with symmetric Gaussian input beams, $A_0(x) = A_{-1}(x) = \exp(-x^2)$ at $Z = 0$, in the absence of both diffraction and dispersion, $\alpha_n = \gamma_n = 0$, was considered. Figure 2 shows the evolution of the transverse profile at the first Stokes frequency. Without dispersion or diffraction in the system, Eq. (3) has an exact and stable solution.[1] This is, of course, reflected in the evolution of the transverse field in each of the frequency channels. The slow convergence of the first Stokes beam in the latter stages of this simulation indicates that at $Z = 100$ the global solution $\{A_n(x, Z) : n = 0, \pm 1, \pm 2, \ldots\}$ is close to a fixed point of the system. However, both the $Z = 100$ solution and the transient evolution that precedes it exhibit strong transverse modulations.

The benefits of using dimensionless variables becomes apparent in the physical interpretation of the solutions

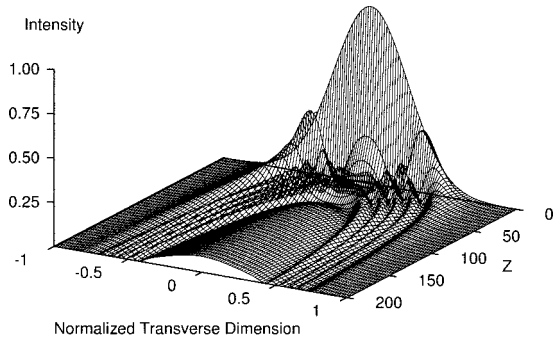

Fig. 2. Evolution of the first Stokes beam over a normalized distance of $Z = Z_{\max} = 200$. Pump energy is rapidly converted into new frequencies during propagation, and the interplay of Raman and finite-beam effects alone is shown to lead to a significant transverse structure ($\alpha_n = \gamma_n = 0$).

calculated. For example, negligible dispersion ($\Delta_1 = 0$ and thus $\gamma_1 = \Delta_1/gI_0 = 0$) implies that the actual value of the SRS gain gI_0 is not specified. Transverse profiles at each $Z = gI_0z$ (the SRS gain–length product) can then be interpreted as applying to any peak beam intensity I_0, provided that a suitable distance z is specified. An alternative viewpoint is that the dependence of the dispersionless plane-wave solution on pump intensity is mapped out across the transverse plane at each Z. The development of spatial structure is most rapid at the center of the beam because the higher light intensity there drives stronger (parametric) frequency conversion. Because Z is defined in terms of the peak input intensity, I_0, the threshold for 1% conversion at beam center is given by the value for planar symmetric pumping $Z = Z_{\text{th}} \simeq 0.2$. This is in marked contrast to the rate of frequency conversion in the wings of the beam. It is this range of conversion rates across the beam that quickly gives rise to a complex transverse structure as the beam evolves. As $Z \to \infty$, the transverse profile converges to a fixed point as the polarization wave becomes quenched owing to gain suppression. When $\alpha_n = 0$, this requires that $\lim_{Z\to\infty}\Sigma_j A_j A_{j-1}{}^* = 0$ at each x; thus locally $P \to 0$ and $\partial A_n/\partial Z \to 0$.

An important global characteristic of the UMRG process is the bandwidth generated. This can be defined as either the number of frequency channels carrying comparable energy, B_N, or the actual frequency range that these channels span, B_ω. Under the above conditions of $\alpha_n = \gamma_n = 0$, B_N converges to $\omega_0/\omega_R \simeq 32$ at $Z \simeq 100$, and thus $B_\omega \simeq \omega_0$, as predicted by dispersionless plane-wave analysis.[1] When a small amount of diffraction is then introduced, we find that it can play an analogous role to dispersion in the system; it can offset exact phase matching and lead to an extension of the longitudinal interaction length.[2] This, in turn, can result in B_N greater than ω_0/ω_R. However, realistic considerations require both diffraction and dispersion to be accounted for.

In plane-wave modeling, a level of dispersion given by $\gamma_1 \simeq 2.75 \times 10^{-3}$ was found to maximize the bandwidth generated.[2] It is necessary to ask how diffraction will affect this optimization. Figure 3 shows the result of varying the pump-beam diffraction length L_D. We have chosen $I_0 = 5$ GW cm^{-2} to yield $\gamma_1 \simeq 2.75 \times 10^{-3}$, whereby $Z = 200$ corresponds to a propagation distance of 2 m. Increasing levels of (relatively strong) diffraction, in the presence of dispersion, is shown to decrease the bandwidth generated. This is an important consideration for experiments that employ tightly focused input beams. Longitudinal dispersive mistunings and transverse diffractive effects appear to contribute to the system in an additive fashion and to push the point of optimum dispersion toward lower γ_1 (and hence higher pump intensities). However, we stress that B_ω may still be of the order of the pump carrier frequency, even when diffraction is appreciable. Another important characteristic of ultrabroadband light is the quality of the resultant multifrequency beam. Figure 4 shows snapshots of the evolution of the total (incoherent) beam intensity $I_\Sigma(x) = \Sigma_j|A_j(x)|^2$ at distances corresponding to $z/L_D = 0.5$ and 1. Although plane-wave analysis is clearly invalid in such cases, the transverse distribution of energy can be seen to remain reasonably axial, and, aside from sharp local peaks, the overall shape corresponds to that of a *single* multifrequency beam.

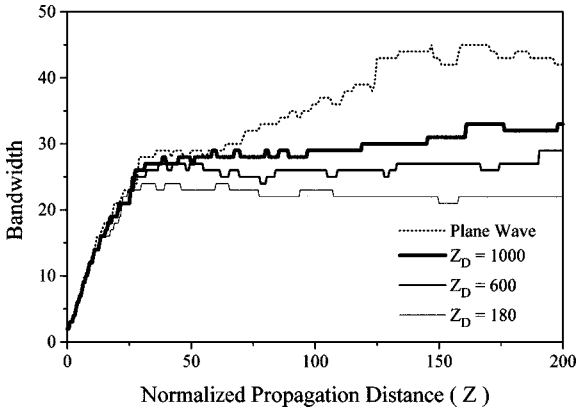

Fig. 3. Bandwidth B_N (in units of the Stokes shift) of 1D transverse multifrequency beams as a function of normalized distance Z. A 2-m chamber of H_2 gas at 1-atm pressure is modeled. Dispersion and diffraction are accounted for ($\alpha_n \neq 0$, $\gamma_n \neq 0$, and Z_D is the normalized diffraction length of the ω_0 pump). The dispersion-optimized plane-wave curve is also shown (dotted).

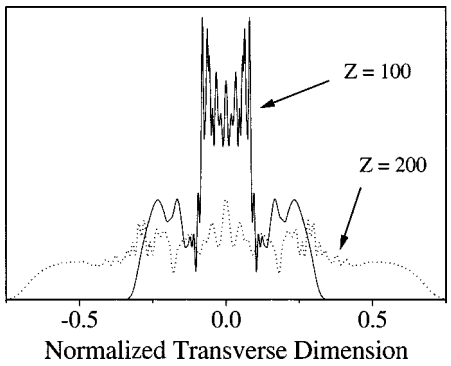

Fig. 4. One-dimensional transverse profiles, at normalized distances $Z = 100$ and $Z = 200$, of the total (incoherent) intensity (I_Σ) of the multifrequency beam. Parameters are for H_2 gas at 1-atm pressure and relatively strong diffraction ($Z_D = 200$).

5. TWO-DIMENSIONAL TRANSVERSE ULTRABROADBAND MULTIFREQUENCY RAMAN GENERATION

The 1D results demonstrate the importance of including diffractive effects in studies of UMRG, but there are few experimental situations for which a single transverse dimension is appropriate. The results presented in the remainder of this paper therefore include propagation effects in two transverse dimensions. We begin these 2D investigations by examining the dependence of bandwidth B_N on the level of mistuning introduced by background dispersion γ_1. Figure 5 shows results at fixed $Z = 60$ for two pump-beam widths, corresponding to normalized diffraction lengths of $Z_D = 180$ and $Z_D = 600$. The difference between these two cases is highlighted by plotting the results on a scale that starts at $B_N = 12$. For fixed

pressure and temperature of the Raman medium, γ_1 is inversely proportional to peak input intensity I_0, and this parameter is also shown in Fig. 5. While it was possible to perform 1D simulations up to $Z_{\max} = 200$, computational memory requirements restrict 2D explorations to $Z_{\max} = 60$. This is because, once a sufficient transverse sampling density is determined, a maximum of 512×512 transverse points in each frequency channel dictates the size of the transverse grids. Diffractive broadening of the interacting beams then imposes an upper limit on the propagation distance that can be accurately modeled.

As suggested by 1D investigations, to obtain 2D beams with bandwidths comparable to those of plane-wave configurations, one generally requires higher input intensities. This can be understood in terms of the evolution of the light intensity at each transverse point. In the plane-wave case, energy launched at a specific transverse point is implicitly confined and remains at that location. In 1D beam configurations, input energy diffracts, and this generally leads to lower intensities in the region where the energy was launched. Progressing to 2D beams, diffraction in an additional transverse direction results in a further reduction in local intensities during propagation. Nevertheless, Fig. 5 reveals the existence of a broad plateau region around $I_0 = 30$ GW cm^{-2}, within which the bandwidth generated is relatively insensitive to the value of pump intensity. We have also verified that this feature appears for values of Z_D that are intermediate to those used in Fig. 5.

By focusing attention on this plateau region, more general conclusions regarding the evolution of the bandwidth generated, and its dependence on pump diffraction length, can be drawn. Hereafter, we consider a fixed value of pump intensity $I_0 = 30$ GW cm^{-2}. Figure 6 charts the growth of bandwidth up to $Z_{\max} = 60$ and shows the effect of varying the input-beam width. For 1 atm of H_2 gas, this pump intensity and normalized propagation distance imply a Raman cell of length 10 cm. Since Z_D is proportional to intensity, the values of normalized diffraction length used in Fig. 3 now correspond to narrower input beams. A comparison with 1D beam evolution reveals that, by focusing down the pumps to narrower beams of higher intensity, bandwidths obtained with 2D beams are only marginally smaller and are still of the order of the pump carrier frequency.

Such physical considerations raise other questions of interest: What role is played by the quality of the input beams, and what are the consequences of launching either converging or diverging beams into the gas chamber? Through further simulations and examination of the initial stages of conversion, we have found that the transverse phase profile of each input beam is rapidly scrambled after entering the Raman medium, and that this renders the detail of the incident phase profile essentially irrelevant. Transverse UMRG is thus robust with respect to the focusing character and to the phase quality of the sources used. This leaves the peak intensity and the beam width of the pumps, along with the total propagation distance, as key parameters for bandwidth optimization.

Typical wavelength distributions of the bandwidth generated are shown in Fig. 7, where the power spectrum

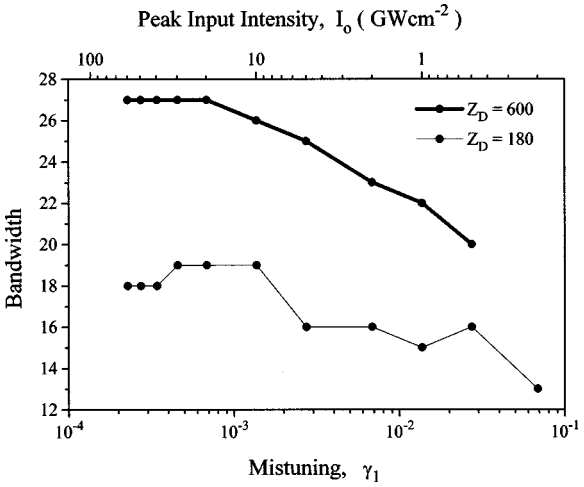

Fig. 5. Dependence of bandwidth B_N of 2D transverse multifrequency beams on the intensity and the diffraction length of the pump beams ($Z = 60$).

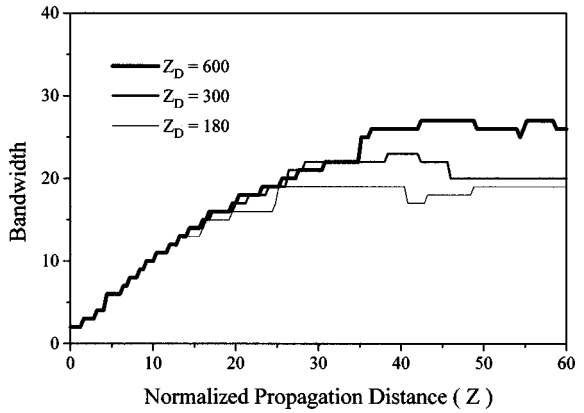

Fig. 6. Evolution of the bandwidth of 2D transverse beams along a 10-cm Raman cell. Three normalized pump-beam diffraction lengths are considered ($I_0 = 30$ GW cm^{-2}).

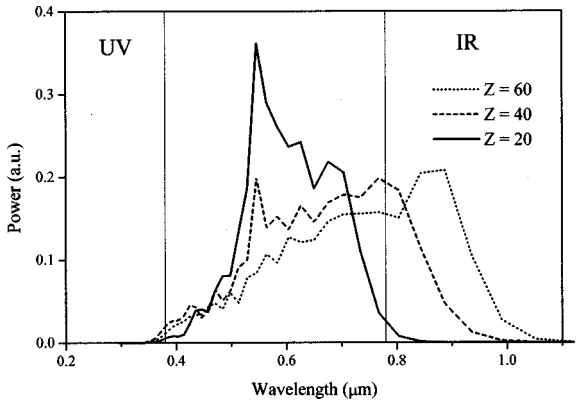

Fig. 7. Evolution of the power spectrum of a multifrequency beam. The limits of the visible spectrum are indicated by two vertical lines. The pump parameters are $I_0 = 30$ GW cm^{-2} and $Z_D = 600$.

(transversally integrated intensity versus wavelength) is plotted at three normalized distances. This particular configuration corresponds to the $Z_D = 600$ curve of Fig. 6 and thus to an input beam diffraction length of 1 m. Two vertical lines are also drawn in Fig. 7 to delimit ultravio-

let (UV), visible, and infrared (IR) regions. The input beams are positioned near the center of the visible spectrum and reside at 0.529 μm and 0.546 μm. This latter wavelength is that of the first Stokes beam and is also associated with the strong peak in both the $Z = 20$ and $Z = 40$ curves. The fact that, in the very first stage of frequency conversion, a large amount of pump energy is transferred into the first Stokes channel appears to have a residual effect on the power spectrum over much more significant distances.

Because parametric processes generate new frequencies in pairs, one could expect that spectra would be roughly symmetrically distributed around the input frequencies. However, Fig. 7 shows that the combined effect of dispersion and diffraction results in bandwidth growth that progressively redistributes power toward the red and IR regions of the spectrum. This feature is made more pronounced by the fact that, whereas each spectrum consists of a comb of equidistant frequencies $\omega_n = \omega_0 + n\omega_R$, on a wavelength scale, Raman lines are not uniformly spaced. The physical origin of asymmetric energy redistribution is that UMRG also involves (phase-insensitive) nonparametric processes that transfer energy only to lower-frequency channels; parametrically generated components can provide strong seeds for this type of downconversion.

To illustrate the transverse profiles of beams in the constituent frequency channels, we consider the case of relatively strong diffraction. Such smaller pump-beam widths generally result in reduced bandwidth, when compared with broader input beams of the same intensity, but diffractive spreading is greater, and this allows the variation of the transverse structure across the Raman spectrum to be inspected more easily. An array of individual intensity profiles is shown in Fig. 8. Moving down column 1, the first two beams are IR, and the next four are in the red region of the visible spectrum. Column 2 is a continuation of column 1 (downward corresponding to increasing frequency), and columns 3 and 4 continue this sequence. The first Stokes and pump frequency channels are at the bottom of column 2 and at the top of column 3, respectively. Many of the beams are found to exhibit complex ring structures. From the 1D results, one can deduce that the origin of these rings lies in the interplay of finite-beam effects and the intensity dependence of Raman conversion. A lack of appreciable modulational instability in the system is also further evidenced, since its presence would tend to break up such rings into necklaces of spatial filaments.

High-order anti-Stokes beams are generated primarily through parametric mechanisms. In particular, for blue and indigo wavelengths (the lower section of column 3 and the top of column 4), beam profiles are generally narrower than those in other regions of the spectrum. This reflects both weaker diffraction in the higher-frequency regime and that near-phase-matching conditions exist when these beams propagate collinearly. At the other end of the spectrum, toward IR, nonparametric effects will be stronger, and diffraction is also much more severe. In the transition from visible to IR frequencies, multiple ring structures begin to disappear and beams assume the shape of a single ring. These rings are bright and relatively wide, thus containing more power than higher-frequency beams. It is their presence that ultimately limits the propagation distances that can be modeled in 2D transverse simulations. Noting from Eq. (3) that when a number of adjacent fields, $n = j - 1$, j, and $j + 1$, become zero and thus the UMRG process is halted, one can infer that conversion is halted in the dark regions enclosed by the IR rings and also that any further downconversion will result in similar doughnut-shaped beams.

Examination of constituent beam profiles provides qualitative snapshots of transverse effects for specific propagation distances and for particular levels of diffraction. A more comprehensive picture is obtained by defining quantities that characterize the overall transverse structure in individual frequency channels and then by studying how these quantities vary with respect to both Z and Z_D. We first define a mean radius R_n, for the intensity distribution in channel n, as

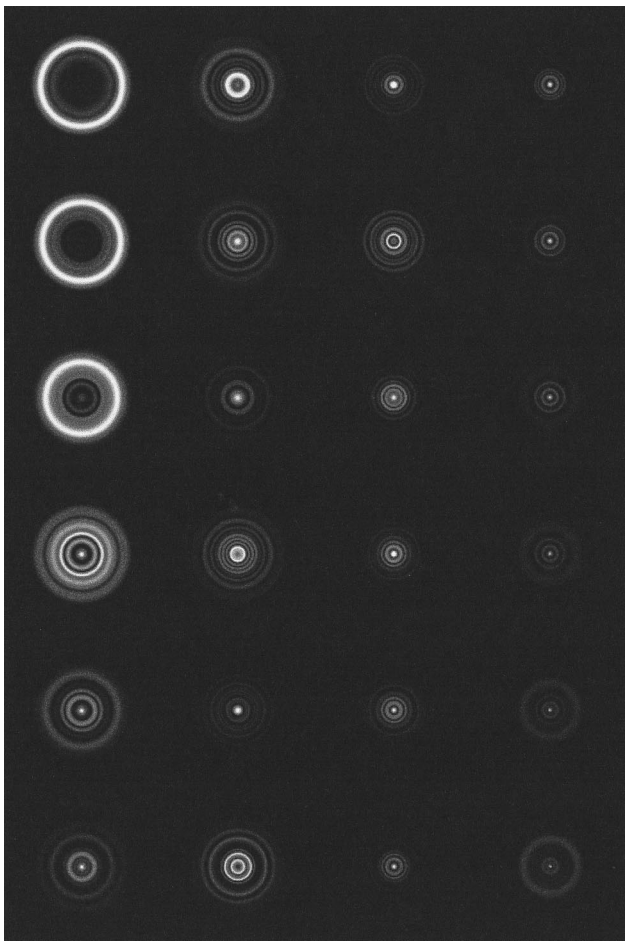

Fig. 8. Transverse intensity profiles of beams within distinct frequency channels ($Z = 60$, $Z_D = 180$, and $I_0 = 30$ GW cm^{-2}). Moving downward through each column, the carrier frequency of the light increases, whereas adjacent columns (moving from left to right) give a continuation of the sequence. In column 1, the beams are in the infrared regime and then progress through the red section of the visible spectrum. Column 2 contains red, orange, yellow, and green beams, whereas column 3 has green, blue, and indigo components. Column 4 spans the spectral region from indigo, through violet, and into the ultraviolet.

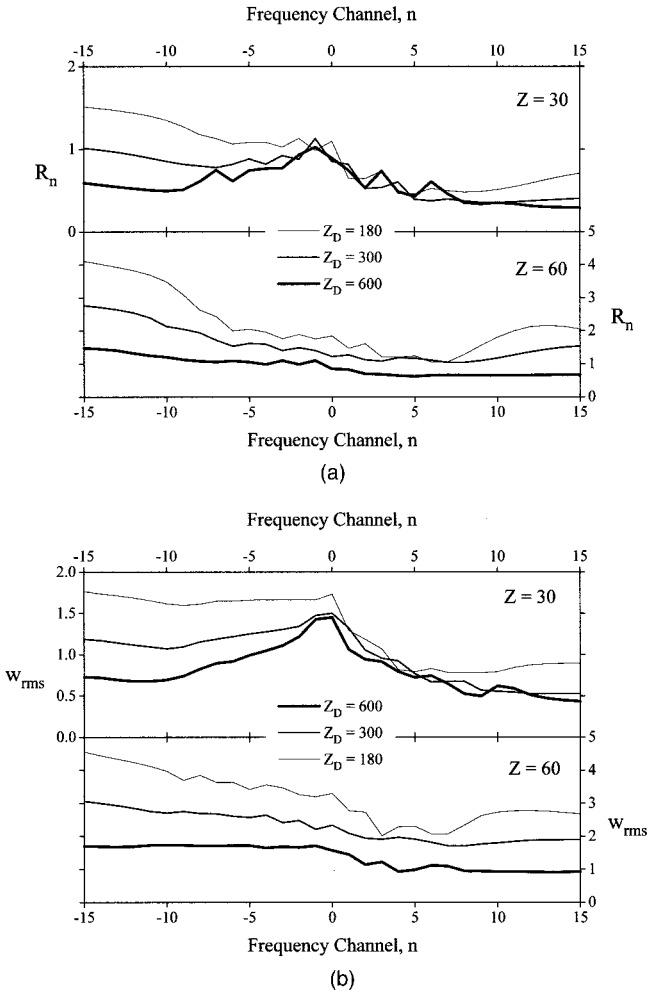

Fig. 9. Variation of beam radii with respect to frequency at two normalized propagation distances ($Z = 30$ and 60) and for three levels of diffraction ($Z_D = 180$, 300, and 600). (a) Mean ring radii R_n, as defined in the text; (b) rms beam widths w_{rms} are plotted.

$$R_n = \frac{\int_0^\infty r^2 |A_n(r)|^2 \mathrm{d}r}{\int_0^\infty r |A_n(r)|^2 \mathrm{d}r}, \tag{11}$$

where r is the radial coordinate in the transverse plane. R_n measures the radius of doughnut-shaped beams or, in the case of multiple ring structures, yields a value for the mean ring radius. Second, we define an rms beam width w_{rms} as the radius within which there is 86% of the beam energy. For a Gaussian amplitude profile, w_{rms} yields the $1/e$ point, and for comparative purposes we normalize values of w_{rms} to those defined by the input beams.

R_n and w_{rms} are plotted as a function of frequency in Figs. 9(a) and 9(b), respectively, where two propagation distances and three input beam widths are considered. The low-frequency ($n < -10$) sections of the $Z = 30$ curves indicate that IR rings also form at earlier stages of propagation, whereas the $Z = 60$ data show that these rings undergo rapid expansion for each level of diffraction considered. The sharp definition of IR rings is reflected in the similarity between the evolution of R_n and w_{rms} in this part of the frequency domain. At higher frequencies, beyond indigo and into UV, diffraction is weaker, but stronger dispersion acts to suppress parametric generation of on-axis beams. Particularly for narrower input beams, such as those shown in Fig. 8 that have $Z_D = 180$, there is a marked increase in beam radii. This feature can be attributed to the formation of the weak rings that can be seen in Fig. 8. Interestingly, Fig. 9 indicates that the phase-matching conditions for the existence of high-frequency rings depend on the presence of both strong dispersion and moderate diffraction.

A comparison of the vertical scales of the $Z = 30$ and $Z = 60$ curves of Fig. 9 reveals that the degree of beam expansion, across the *whole* frequency range, is much larger than one would expect on the basis of the pump diffraction lengths. This rapid and global spreading merits further investigation. In Fig. 10, we quantify the degree to which the whole multifrequency beam diffracts by plotting the evolution of the rms width that defines 86% of the total intensity $I_\Sigma(x)$. Results for three pump diffraction lengths are displayed, along with a curve for free-space propagation of the narrowest input beam considered (shown dotted). These data make it abundantly clear that a notional Gaussian pump beam parametrization is misleading, as it grossly underestimates (by approximately two orders of magnitude) the true extent of diffractive spreading. Because a diffraction length is generally proportional to the square of the characteristic scale of a transverse structure, one could explain this difference in terms of additional spatial structure that is approximately an order of magnitude smaller than the input-beam width. In fact, such a structure does arise from the interplay of UMRG and finite-beam effects (see Fig. 2). Moreover, as bandwidth is generated, the global beam radius will be heavily weighted by the relatively powerful IR rings, and these components experience strong diffraction owing to the frequency dependence of the α_n coefficients.

The data of Figs. 9 and 10 could also be interpreted in terms of the spatial quality M_n^2 of each constituent beam,

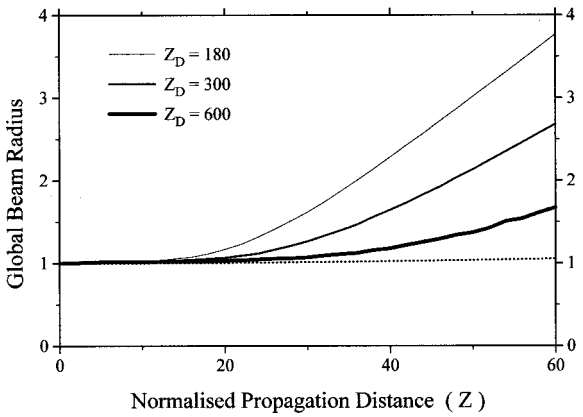

Fig. 10. Evolution of the rms beam radius of the whole multifrequency beam with respect to normalized propagation distance for three levels of diffraction ($Z_D = 180$, 300, and 600). The corresponding evolution for free-space propagation of a Gaussian beam at the pump frequency and with $Z_D = 180$ is also shown (dotted curve).

giving the number of times that each beam is wider than an ideal Gaussian beam of the same waist. Indeed, these beam-quality parameters could be incorporated into an alternative definition of $L_D^{(n)}$, the diffraction length for each frequency channel, by simply letting $\omega_n \rightarrow \omega_n / M_n^2$ in the expression for $L_D^{(n)}$.

6. CONCLUSIONS

In this paper we have presented results from simulations of ultrabroadband multifrequency Raman generation (UMRG). Key concepts and terminology were introduced through analysis and modeling of plane-wave UMRG. The importance of symmetric two-color pumping was highlighted in this context. Considering only one transverse dimension, we reported an absence of modulational instabilities but that finite-beam effects alone (without diffraction) result in significant transverse effects. For both 1D and 2D transverse beams, the evolution and optimization of bandwidth were explored with respect to the intensity and width of the input beams. Results were found to be surprisingly insensitive to either the focusing character or the phase quality of the pump beams.

We showed that beam diffraction generally leads to a requirement of higher input intensities, over that of plane-wave configurations. However, even when transverse effects are fully taken into account, bandwidths of the order of the carrier frequency that span the whole visible spectrum and beyond result. This conclusion is consistent with experiments[7–13] that have involved a range of different Raman systems and that have similarities to the specific configuration modeled here. The evolving power spectra and beam shapes in individual frequency channels have been examined and explained in terms of the constituent parametric and nonparametric process, phase-matching conditions, and the frequency dependence of diffractive coupling lengths. We also examined the dependencies of mean ring radii and rms beam radii of light profiles at individual frequencies and have identified distinct regimes within the generated Raman spectra.

Finally, it was shown that diffraction of the UMRG beam as a whole is much greater than one would expect from the parameters of the Gaussian input beams. This was interpreted in terms of the interplay of finite beams and the intensity dependence of Raman conversion, along with particular features of the transverse effects reported. Such nonlinear beam broadening, which could be called Raman defocusing, is evidently an important effect in high-power beam propagation. In the particular context of UMRG in air at atmospheric pressure,[5] the Raman gain coefficient is much lower than the value for H_2 gas, and this dictates that longer propagation paths need to be considered. One consequence of these greater distances is that self-focusing effects also need to be taken into account. However, one expects there to be a trade-off between beam narrowing owing to nonlinear refraction and beam broadening in the form of Raman defocusing in atmospheric UMRG.

ACKNOWLEDGMENTS

The authors wish to acknowledge useful discussions with Leonid L. Losev, Andrey P. Lutsenko, and Mick J. Shaw. This work was supported in part by Engineering and Physical Sciences Research Council grant GR/L90583.

*Permanent address: Photonics and Nonlinear Science Group, Joule Physics Laboratory, School of Sciences, University of Salford, Salford M5 4WT, UK

†Corresponding author: G. H. C. New, Laser Optics & Spectroscopy Group, The Blackett Laboratory, Imperial College of Science, Technology and Medicine, Prince Consort Road, London SW7 2BW, UK. Telephone: +44 (0)20 7594 7791. Fax: +44 (0)20 7594 7714. E-mail: g.new@ic.ac.uk.

REFERENCES

1. L. L. Losev and A. P. Lutsenko, "Parametric Raman laser with a discrete output spectrum equal in width to the pump frequency," Quantum Electron. **23**, 919–926 (1993).
2. G. S. McDonald, G. H. C. New, L. L. Losev, A. P. Lutsenko, and M. J. Shaw, "Ultrabroad bandwidth multi-frequency Raman generation," Opt. Lett. **19**, 1400–1402 (1994).
3. G. S. McDonald, G. H. C. New, L. L. Losev, A. P. Lutsenko, and M. J. Shaw, "On the generation of ultrabroad bandwidth light for inertial confinement fusion," Inst. Phys. Conf. Ser. **140**, 85–88 (1995).
4. G. S. McDonald, "Ultrabroad bandwidth multi-frequency Raman soliton pulse trains," Opt. Lett. **20**, 822–824 (1995).
5. G. S. McDonald, G. H. C. New, L. L. Losev, and A. P. Lutsenko, "On the generation of ultra-broad bandwidth light in air at atmospheric pressure," J. Phys. B **30**, L719–L725 (1997).
6. G. S. McDonald, Yuk-Ming Chan, G. H. C. New, L. L. Losev, and A. P. Lutsenko, "Competing nonlinear effects in multi-frequency Raman generation," J. Mod. Opt. **45**, 1099–1110 (1998).
7. T. Imasaka, S. Yamanishi, S. Kawasaki, and N. Ishibashi, "Multi-frequency laser emission generated by two-color stimulated Raman effect using a single-frequency laser beam and a dye–Raman composite resonator," Appl. Opt. **32**, 6633–6637 (1993).
8. Y. Irie and T. Imasaka, "Generation of vibrational and rotational emissions by four-wave Raman mixing using an ultraviolet femtosecond pump beam," Opt. Lett. **20**, 2072–2074 (1995).
9. H. Kawano, C. H. Lin, and T. Imasaka, "Generation of high-order rotational lines by four-wave Raman mixing using a high-power picosecond Ti:sapphire laser," Appl. Phys. B **63**, 121–124 (1996).
10. C. H. Lin, T. Ohnishi, and T. Imasaka, "Vibrational stimulated Raman emission from dibromomethane as seed beam for four-wave rotational Raman mixing in hydrogen," Jpn. J. Appl. Phys. **36**, L412–L414 (1997).
11. H. Kawano, Y. Ishidzu, and T. Imasaka, "Generation of more than 40 rotational lines by picosecond and femtosecond Ti:sapphire laser for Fourier synthesis," Appl. Phys. B **65**, 1–4 (1997).
12. H. Kawano, Y. Hirakawa, and T. Imasaka, "Generation of high-order rotational lines in hydrogen by four-wave Raman mixing in the femtosecond regime," IEEE J. Quantum Electron. **34**, 260–268 (1998).
13. T. Mori, Y. Hirakawa, and T. Imasaka, "Role of supercontinuum in the generation of rotational Raman emission based on stimulated Raman gain and four-wave Raman mixing," Opt. Commun. **148**, 110–112 (1998).

14. A. P. Hickman, J. A. Paisner, and W. K. Bischel, "Theory of multiwave propagation and frequency conversion in a Raman medium," Phys. Rev. A **33**, 1788–1797 (1986).
15. A. P. Hickman and W. K. Bischel, "Theory of Stokes and anti-Stokes generation by Raman frequency conversion in the transient limit," Phys. Rev. A **37**, 2516–2523 (1988).
16. A. Flusberg, S. Fulghum, H. Lotem, M. Rokni, and M. Tekula, "Multiseed stimulated rotational Raman scattering for wave-front control," J. Opt. Soc. Am. B **8**, 1851–1875 (1991).
17. G. P. Agrawal, *Nonlinear Fiber Optics* (Academic, London, 1989).
18. Y. R. Shen and N. Bloembergen, "Theory of stimulated Brillouin and Raman scattering," Phys. Rev. **137**, A1787–A1805 (1965).
19. C. Reiser, T. D. Raymond, R. B. Michie, and A. P. Hickman, "Efficient anti-Stokes Raman conversion in collimated beams," J. Opt. Soc. Am. B **6**, 1859–1869 (1989).